Water Practice & Technology

IWA PUBLISHING

Water Practice & Technology Vol 19 No 3, 1047 doi: 10.2166/wpt.2024.032

Mechanism and performances of methyl orange and Congo red adsorption by MnO_2–PVP composite

Afsar Khan [a,*], Muhammad Arif[b], Zhengwei Han[a], Yu Xie[a] and Chenquan Ni[a]

[a] School of Minerals Processing and Bioengineering, Central South University, Changsha 410083, China
[b] College of Chemistry and Chemical Engineering, Central South University, Changsha 410083, China
*Corresponding author. E-mail: afsarkhan@csu.edu.cn;

AK, 0000-0002-6217-3260

ABSTRACT

Azo dyes are commonly used in textile industries; however, when these dyes cross the permissible limit set by the World Health Organization, they produce many health issues related to the brain, liver, kidneys, respiration, and sexual system. Herein, polyvinyl pyrrolidone (PVP)-supported manganese oxide (MnO_2) was studied for azo dye removal from an aqueous medium. The adsorption mechanism study demonstrated that the dye adsorption by MnO_2–PVP composite was not only due to the electrostatic force of attraction but also involved the ion exchange amid the hydroxide group and dye molecules. The surface area of the composite (120 $m^2\ g^{-1}$) was larger than that of metal oxide (102 $m^2\ g^{-1}$). The point of zero charge and surface area were improved from 5.2 and 102 to 5.6 and 120 $m^2\ g^{-1}$, respectively. The dye removal capacity of MnO_2–PVP composite was significantly higher than that of plain MnO_2. The film diffusion control adsorption kinetic mechanism and the kinetic data were well fitted to the pseudo-second-order equation. Experiments were conducted as a function of initial dye concentration (5–200 mg L^{-1}), pH (3–10), temperature (298–328 K), and adsorbent dosage (0.05–0.4 g) in batch adsorption systems. The thermodynamic investigations confirm that the dye adsorption process was endothermic in nature.

Key words: adsorption mechanism, azo dyes, pseudo-second-order kinetic equation, solvothermal method, surface area

HIGHLIGHTS

- The polyvinyl pyrrolidone (PVP)/MnO_2 composite was synthesized by the solvothermal method.
- The adsorption capacity of PVP/MnO_2 was higher than plain metal oxide.
- Detail adsorption mechanism was studied by kinetic models.
- PVP/MnO_2 could be used as a candidate in the water filtration assembly of dyes.
- Detail characterization of the plain and composite metal oxides was performed.

GRAPHICAL ABSTRACT

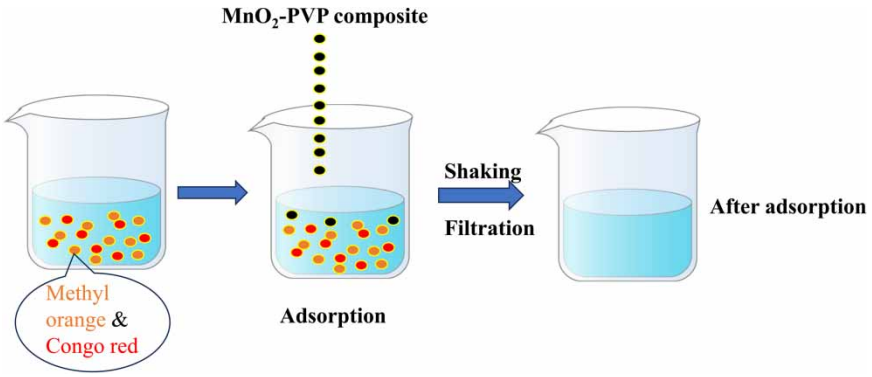

1. INTRODUCTION

Drinking water contamination is one of the environmental problems all over the world and particularly in big cities of our country (Peshawar, Karachi, Lahore, and Faisalabad), which made the general public at risk due to intolerable levels of dyes in the water system and food webs (Parveen & Rafique 2018; Mon *et al.* 2019; Kabuba & Banza 2021; Khan *et al.* 2022; Abugu *et al.* 2023). Azo dyes, containing one or more azo group ($N=N$), are the most widely used dyes such as methyl orange and Congo red. However, when these dyes cross the permissible limit set by World Health Organization, it produces many health issues related to the brain, liver, kidneys, respiration, and sexual system (Nuengmatcha *et al.* 2023; Oladoye *et al.* 2023). Even trace amount of these dyes also shows high visibility, reducing the penetration of sunlight in water and inhibiting the oxygen content and the photosynthesis process. Furthermore, aromatic amines with azo group have been shown to be carcinogenic to animals and human beings (Aliabadi & Mahmoodi 2018; Naseem *et al.* 2018; Zhang *et al.* 2019). Therefore, these dyes must be treated before and after entering the general public drinking water.

Activated carbon is a familiar adsorbent for decontamination of drinking water from toxic organic pollutants; however, activated carbon has various limitations such as slow kinetics and lower capacity for micro-pollutants, and regeneration requires energy (Alsbaiee *et al.* 2016). Various traditional adsorbents can solve drawbacks up to some extent. However, controlling the adsorbent surface (point of zero charge (PZC)) and its surface area toward the high adsorption is fairly difficult due to the complex structure of dyes. For this approach, finding a highly selective sustainable adsorbent for researchers is desired.

Polyvinyl pyrrolidone (PVP) is frequently exercised as a surfactant due to nontoxicity and biocompatibility and changed the exposed crystal facets. It is frequently used as a stabilizer and controls the surface configuration. PVP efficiently enhances the percentage of exposed surface area. Our current research findings are concerned with the adsorption of carcinogenic and mutagenic azo dyes from the aqueous medium by newly prepared PVP-modified MnO_2 with high efficiency. A detailed investigation of the process was carried out to find the adsorption mechanism by composite materials. Kinetic and thermodynamic investigation helps us to probe into the adsorption mechanism during the adsorption of methyl orange and Congo red.

2. MATERIALS AND METHODS

2.1. Chemicals and reagents

All the chemicals (methyl orange, Congo red, NaOH, HCl, and $NaNO_3$) and solvents (distilled water, ethanol, and n-hexane) were used as supplied with no additional purification. A total of 1,000 mg L^{-1} stock solution of dyes was prepared. Buffers, NaOH (0.1–0.5 M), and HCl (0.1–0.5 M) were employed for pH adjustment. The dye solutions ranged from 5 to 200 mg L^{-1} for all experiments. All chemicals utilized were research grade in purity, and distilled water was used in solution preparation in the course of the investigation.

2.2. Synthesis of composite material

The composite material was synthesized by the previously applied hydrothermal method (Li *et al.* 2015; Khan *et al.* 2022) with changes. A 0.5 M MnO_2 and 0.1 M PVP were mixed in 100 ml beaker and stirred for 2 h at room temperature (298 K) until the solution became clear. The white precipitate was centrifuged, washed with DI water and ethanol, and dried at 80 °C in the oven for 6 h before further processing.

2.3. Characterization of MnO_2–PVP composite

The morphologies and elemental analysis of the as-formed materials were determined by scanning electron microscope (model: JSM 5910, JEOL, Japan) and Energy Dispersive X-ray Spectrometer (EDX) (model: INCA 200, Oxford Instruments, England). The surface area was calculated by Quantachrome Nova 2200e (Quantachrome Instruments, USA). The geometry was characterized by the X-ray diffraction (XRD) model JDX-3532 (JEOL). The thermo-gravimetric analysis (TGA) was performed by a TGA analyzer (Perkin Elmer, USA; model: Pyris Diamond Series TG/DTA). Fourier-transform infrared spectroscopy (FTIR) was performed by IR (model: Shimadzu 8201 PC; Shimadzu, Japan). The PZC of materials was determined experimentally by the salt addition method.

2.4. Adsorption experimentations

The mixture of adsorbent (0.05–0.4 g) and 40 ml of dye of various concentrations (5–200 mg L^{-1}) was placed in a shaker for various intervals of time (1–2,880 min). The pH (3–10) was adjusted, and the temperature was in the

range of 298–328 K. After flirtation, the dye concentration was analyzed by Vernier Spectrovis plus fluorescence. The equilibrium concentration (C_e) of dye was calculated with the help of a calibration curve.

3. RESULTS AND DISCUSSION

3.1. Characterization of MnO_2 and MnO_2–PVP composite

3.1.1. Surface area

The surface areas of MnO_2 and MnO_2–PVP composite were calculated by the adsorption–desorption method, and the surface area of PVP-supported MnO_2 was found to be 120 $m^2\ g^{-1}$, while for MnO_2, it was 102 $m^2\ g^{-1}$. The pore size and the surface area of plain oxide (3.162 nm and 102 $m^2\ g^{-1}$) were lower than those of supported oxide (3.30 nm and 120 m^2/g). The difference in surface areas and porosity of the two materials is due to the attachment of the organic component (PVP) to the inorganic component (MnO_2) where the porosity of carbon plays a role in higher surface area and particle porosity after composite formation, and hence, the material becomes carbonaceous (Bhatnagar & Jain 2005).

3.1.2. Point of zero charge

The PZC is the pH at which the electrical charge on the surface is zero. Above that PZC point, the charge on the surface is negative and, below that, the surface is positively charged that influences the adsorption of anionic and cationic species. Figure 1(a) shows the PZC of MnO_2 and its composite at pH 5.2 and 5.4, respectively, which is close to the value (i.e., 4.9) reported for adsorbents in soil by Miyittah *et al.* (2016). The small change in PZC of composite compared to MnO_2 confirms the physical interaction between MnO_2 and PVP polymer. Higher PZC value means the surface zero charge is shifted to a higher value and the availability of positive charged surface increased, which is more favorable for adsorption of anionic dyes like methyl orange and Congo red.

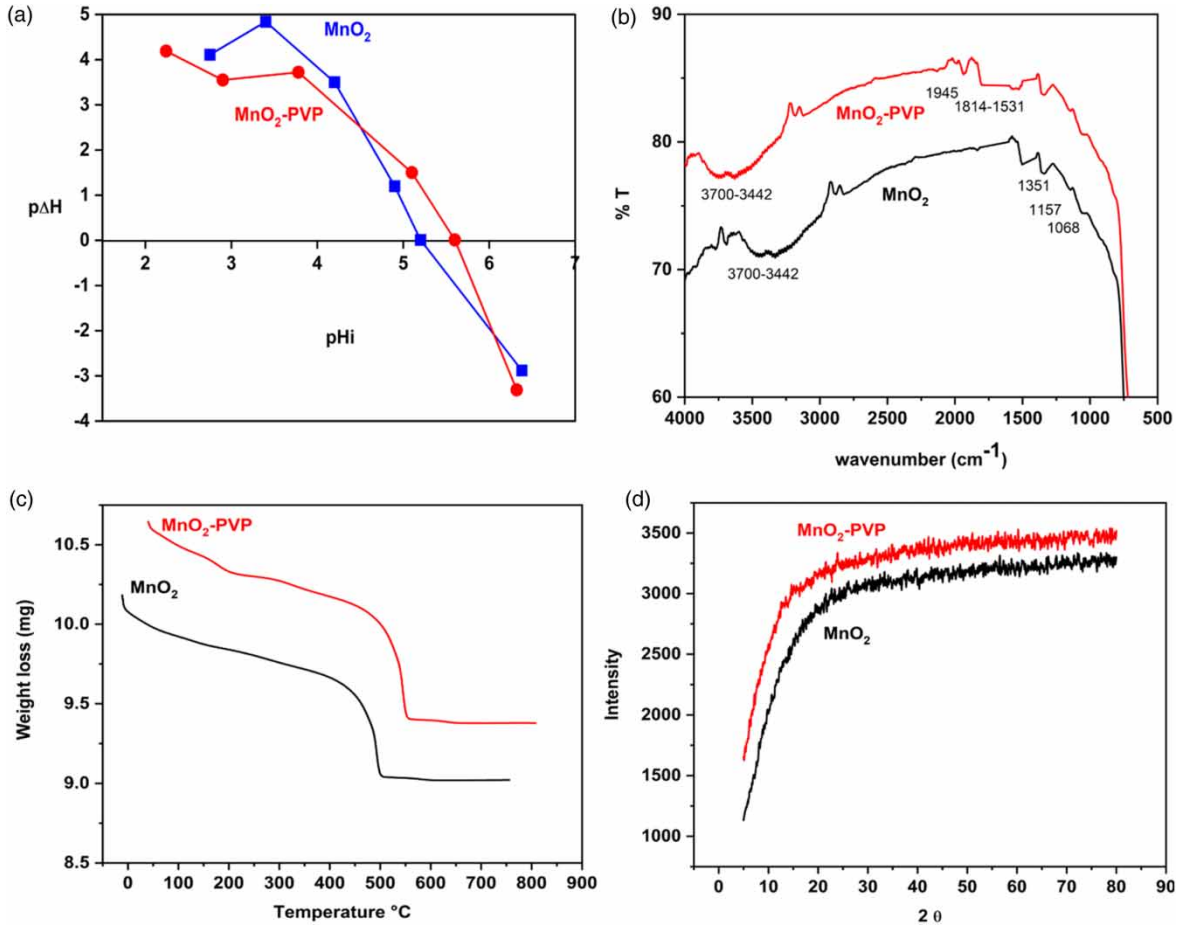

Figure 1 | PZC (a), FTIR (b), TGA (c), and XRD (d) of MnO_2 and MnO_2–PVP composite.

3.1.3. FTIR analysis

The FTIR study provides information about functional groups available at the solid surface. A strong peak at 525 cm^{-1} in MnO_2 shows the stretching vibration of the MnO bond (Figure 1(b). The absorption bands at 1,068, 1,157, and 1,351 cm^{-1} confirm the O-H bending vibrations connected with manganese atoms. Furthermore, the band from 3,700 to 3,443 cm^{-1} for metal oxide and polymer-loaded metal oxide is allocated to O-H stretching, whereas the band at 1,814–1,531 in the composite corresponds to the C-O stretching and the peak at 1,945 cm^{-1} is due to hydrogen bonding in composite, which proves the attachment of organic groups on the surface of composite (Saeed *et al.* 2021; Song *et al.* 2021). The contact is due to electron pair donation to cation from carbonyl oxygen, and a complex formation amid cation and nitrogen (Rose *et al.* 2013).

3.1.4. TGA analysis

The TGA is a thermal technique in which the weight loss of material is monitored at different intervals of time with a temperature from 30 to 800 °C. It tells about the thermal stability of an adsorbent. The TGA was performed at 30–800 °C. The weight loss seems to be similar in both cases (Figure 1(c)). The first stage of weight loss was the same as pure PVP and appeared below 180 °C, which was because of evaporation of physically adsorbed moisture. A second weight loss attributed to chemisorbed water and appears at 200–400 °C. The third stage weight loss at higher temperature (450–550 °C) shows the oxygen emission by the reactions (Kim & Popov 2003):

$$2MnO_2 \rightarrow MnO_2 + 1/2O_2$$
$$3MnO_2 \rightarrow 3Mn_3O_4 + 1/2O_2$$

3.1.5. XRD analysis

XRD is frequently used to define the crystalline, amorphous, or semi-crystalline nature of the materials and also provides an idea about the unit cell dimensions. The XRD spectra of metal oxide and PVP-loaded metal oxide (Figure 1(d)) confirm the poor crystallinity of both materials, and similar results were presented by Yuan *et al.* (2015) for the MnO_2/PPy composite.

3.2. Batch adsorption study

3.2.1. Kinetic study of adsorption

Kinetic parameters of azo dye adsorption were investigated at pH 5 at various temperatures (298–328 K). No more adsorption was observed once the process reached adsorption equilibrium. The quantity of dye adsorbed is plotted versus time, which is shown in Figure 2(a) and 2(b), respectively. The figures show that the equilibrium was reached after 150 min for methyl orange and 50 min for Congo red. The rate of adsorption was fast initially, and the Congo red adsorption was double compared to methyl orange at a given pH due to the structure of Congo red azo dye. Furthermore, no significant removal was observed behind equilibrium time. Figures show that the adsorption increases with the temperature, which confirms the endothermic nature of the process. The high adsorption is due to the movement of molecules at high temperature (328 K) (Khan *et al.* 2020a).

3.2.2. Pseudo-first-order model

The pseudo-first-order expression is presented as follows:

$$\frac{1}{q_t} = \frac{1}{q_e} + \frac{k_1}{q_e t} \tag{1}$$

where q_e and q_t (mol/g) are quantity of dye adsorbed at equilibrium and time (t) respectively, and k_1 is the rate constant. The values of q_e and k_1 can be calculated from the graph amid $(1/q_t)$ versus $(1/t)$ (not shown). In the current work, the calculated theoretical value of q_e from the pseudo-first-order expression is inconsistent with current experimental data (Tables 1 and 2), which confirms the nonapplicability of this model.

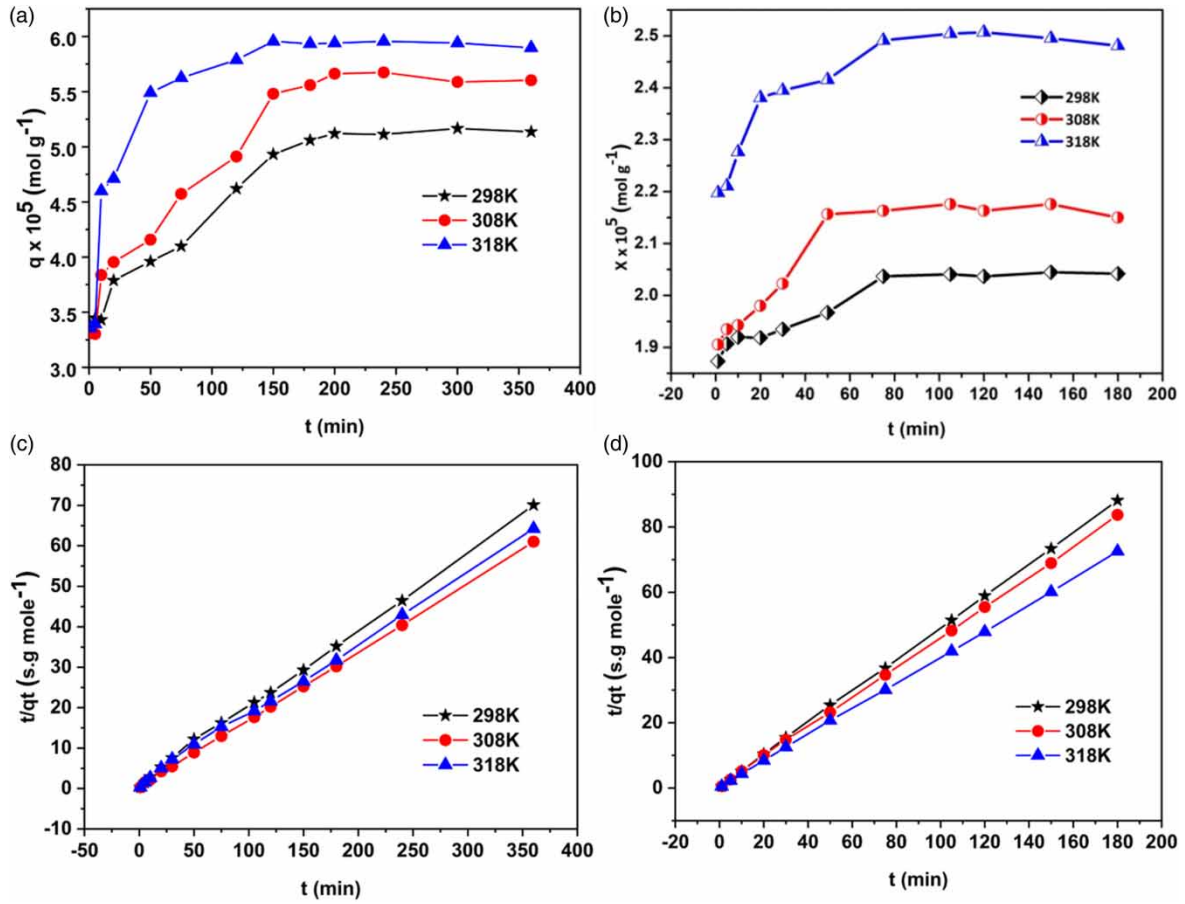

Figure 2 | Kinetics of methyl orange (a), and Congo red (b), pseudo-second-order plot for methyl orange (c), and Congo red (d) on MnO_2–PVP composite at pH 5.

Table 1 | Kinetic parameters for methyl orange adsorption at pH 5

Pseudo-first-order parameters			Pseudo-second-order parameters				
Temperature (K)	Experimental $q_e \times 10^5$ (mol g^{-1})	Theoretical $q_e \times 10^5$ (mol g^{-1})	k_1 min^{-1}	R^2	k_2 (g min^{-1} mol^{-1})	Theoretical $q_e \times 10^5$ (mol g^{-1})	R^2
298	4.62	3.47	0.399	0.35	0.038	5.24	0.99
308	5.62	4.83	0.561	0.44	0.063	5.98	0.98
318	5.48	4.47	0.738	0.61	0.077	5.74	0.99

Table 2 | Kinetic parameters for Congo red adsorption at pH 5

Pseudo-first-order parameters			Pseudo-second-order parmeters				
Temperature (K)	Experimental $q_e \times 10^5$ (mol g^{-1})	Theoretical $q_e \times 10^5$ (mol g^{-1})	k_1 min^{-1}	R^2	k_2 (g min^{-1} mol^{-1})	Theoretical $q_e \times 10^5$ (mol g^{-1})	R^2
298	2.036	1.89	0.074	0.40	0.517	2.053	0.99
308	2.162	1.99	0.121	0.40	0.490	2.177	0.98
318	2.491	2.03	0.125	0.15	0.504	2.505	0.99

3.2.3. Pseudo-second-order model

The pseudo-second-order equation is written in the following form:

$$\frac{t}{q_t} = \frac{1}{k_2 q_e^2} + \frac{t}{q_e} \tag{2}$$

where q_t and q_e (mole/g) are dye adsorbed at time (t) and at equilibrium, respectively, and k_2 (g/min/mol) is the rate constant. The graph of t/q_t versus t gives the straight line for adsorption of dyes (Figure 2(c) and (d)). The q_e experimental, q_e calculated, and R^2 values are near to unity (Tables 1 and 2) and verify the applicability of this model. The process is physical in nature in the case of Congo red as the k_2 value decreases with an increase in temperature (298–328 K), and equilibrium is reached at low temperature (Table 2), while for methyl orange, the opposite trend is observed (Table 1). The k_2 values of Congo red are greater in comparison with methyl orange and show the fast adsorption of Congo red (Khan *et al.* 2020a).

3.3. Adsorption mechanism

3.3.1. Intraparticle diffusion model

The kinetic data were used to certify the adsorption mechanism by the intraparticle diffusion model. The linear form is shown as follows:

$$q_t = K_d t^{1/2} + C \tag{3}$$

where C (mg/g) is the boundary layer thickness and K_d is diffusion constant [mg/g $\text{min}^{0.5}$], and the higher value of C shows a larger boundary layer effect. Özacar & Şengil (2005) also observed such types of multilinearity plots for the sorption of complex yellow onto the pin sawdust at 298 K. They assigned the first portion to the external, while the second portion was assigned to the gradual adsorption stage, where the rate-controlling step was the intraparticle diffusion.

If the graph of q_t versus $t^{1/2}$ passes from origin and linear, then the intraparticle diffusion is the rate-determining step. Figure 3(a) and 3(b) shows that the deviation from origin indicates the pore diffusion model is not the rate-controlling step. The transfer rates in both initial and final stages cause this deviation. R^2 values (Tables 3 and 4) for both dyes confirm the applicability of the intraparticle diffusion but, because of the intercept C, the lines did not pass through the origin, which identify the existence of boundary layer effect and explained that this model is not the rate-controlling step in overall elimination process. As the K_d values increase with an increase in temperature (298–328 K) due to a change in viscosity of the mixture at high temperature (328 K), which facilitates molecular diffusion into pores of surface (Venkatesha *et al.* 2012).

3.3.2. Boyd model

The Boyd model was used for the kinetic data to determine the real rate-determining step. The equation is given as follows.

$$F = 1 - \left(\frac{6}{\pi^2}\right) \sum_{m}^{1} \left(\frac{1}{m^2}\right) \exp(-m^2 Bt) \tag{4}$$

where F is fractional achievement of equilibrium at time (t), which is shown by the following relation:

$$F = \frac{q_t}{q_e} \tag{5}$$

Equation (5) can be written in the following form:

$$F = \text{values} \ > 0.85 \ Bt = \ -0.4977 - \ln(1 - F) \tag{6}$$

and

$$F \text{ values} \ < 0.85 \ Bt = \left[\sqrt{\pi} - \sqrt{\pi - \frac{\pi^2 F}{3}}\right]^2 \tag{7}$$

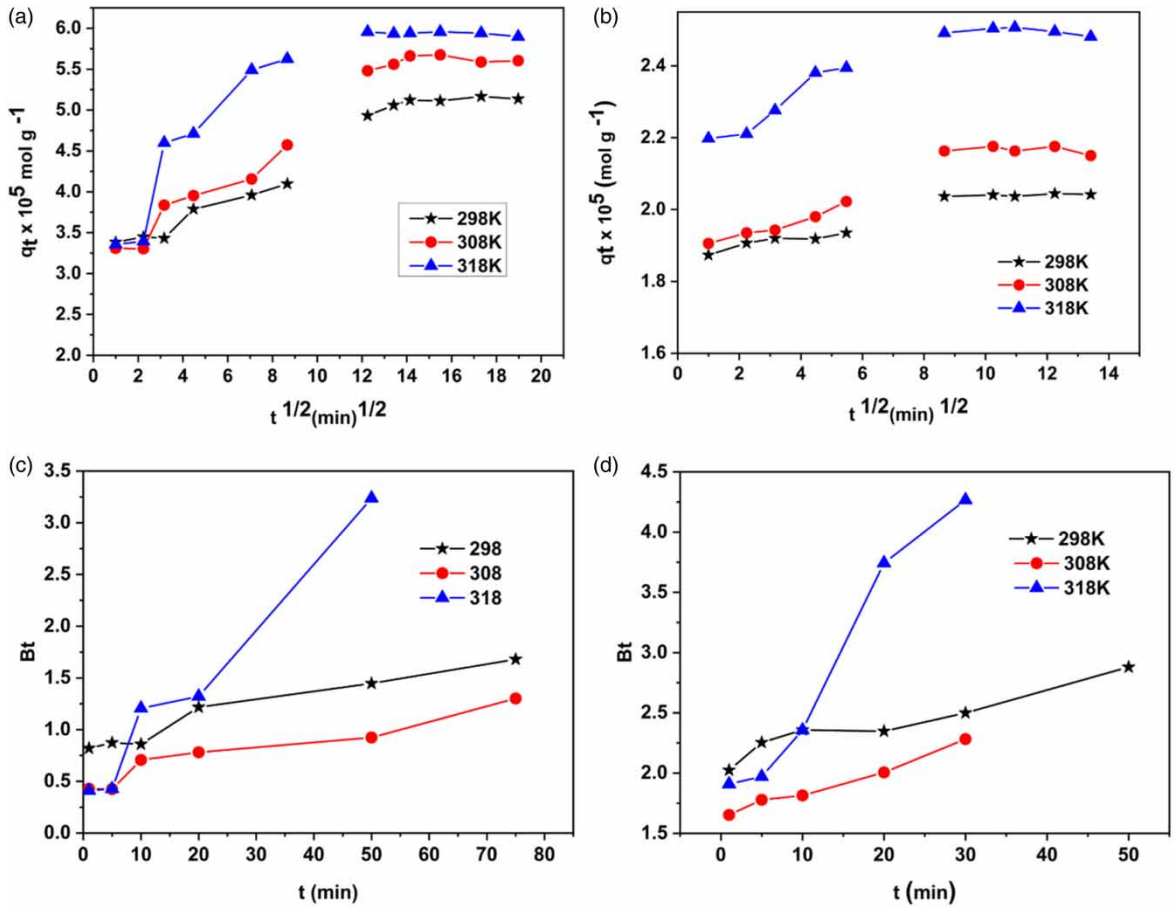

Figure 3 | Intraparticle diffusion plots for methyl orange (a), Congo red (b), Boyd plot for methyl orange (c), and Congo red (d) on MnO_2–PVP composite at pH 5.

Table 3 | Intraparticle model parameters for methyl orange at pH 5

Temperature (K)	$K_d \times 10^7$ (mol g^{-1} min$^{-0.5}$)	R^2
298	19.1	0.97
308	21.1	0.94
318	7.1	0.91

Table 4 | Intraparticle model parameters for Congo red at pH 5

Temperature (K)	$K_d \times 10^7$ (mol g^{-1} min$^{-0.5}$)	R^2
298	2.43	0.91
308	2.06	0.97
318	5.41	0.98

where q_e is adsorbed dye by PVP-modified MnO_2 at equilibrium (mole/g), q_t is adsorbed dye onto the composite at time (t), F is the fraction of dye adsorbed at any time (t), and B_t is function of F. Figure 3(c) and 3(d) shows that the plots did not go through the origin, which confirms that the adsorption is mostly controlled by external diffusion (film diffusion) (Mahmood *et al.* 2016).

3.4. Effect of various parameters

3.4.1. Effect of concentration

The initial dye concentration affects dye elimination efficiency indirectly by either decreasing or increasing the availability of binding sites on the adsorbent surface. There is an immediate relationship between the percentage removal of dyes and the initial dye concentration in adsorption systems. Generally, an increase in the initial dye concentration in the solution will cause the adsorption sites on the adsorbent surface to become saturated, which eventually leads to a decrease in the removal efficiency. The effect of initial concentration on the adsorption of methyl orange and Congo red by MnO_2–PVP composite was investigated with varying solution concentrations (5–200 mg L^{-1}) using 0.1 g adsorbent dose. It could be seen from Figure 4(a) that the percent removal of dye was decreased, while the specific dye uptake was increased with the increasing concentration. The figure shows that the driving force from the concentration gradient results in the higher dye elimination at a higher concentration. The percentage of adsorption goes down from 96.5 to 45.7% for Congo red and from 70 to 30% for methyl orange, with increasing the initial concentration of dye from 5 to 200 mg L^{-1}. This is due to a larger mass-driving force at high concentration that helps to overcome the mass transfer control. In addition, aggregation occurred on the surface at a high concentration (Mahmood *et al.* 2016).

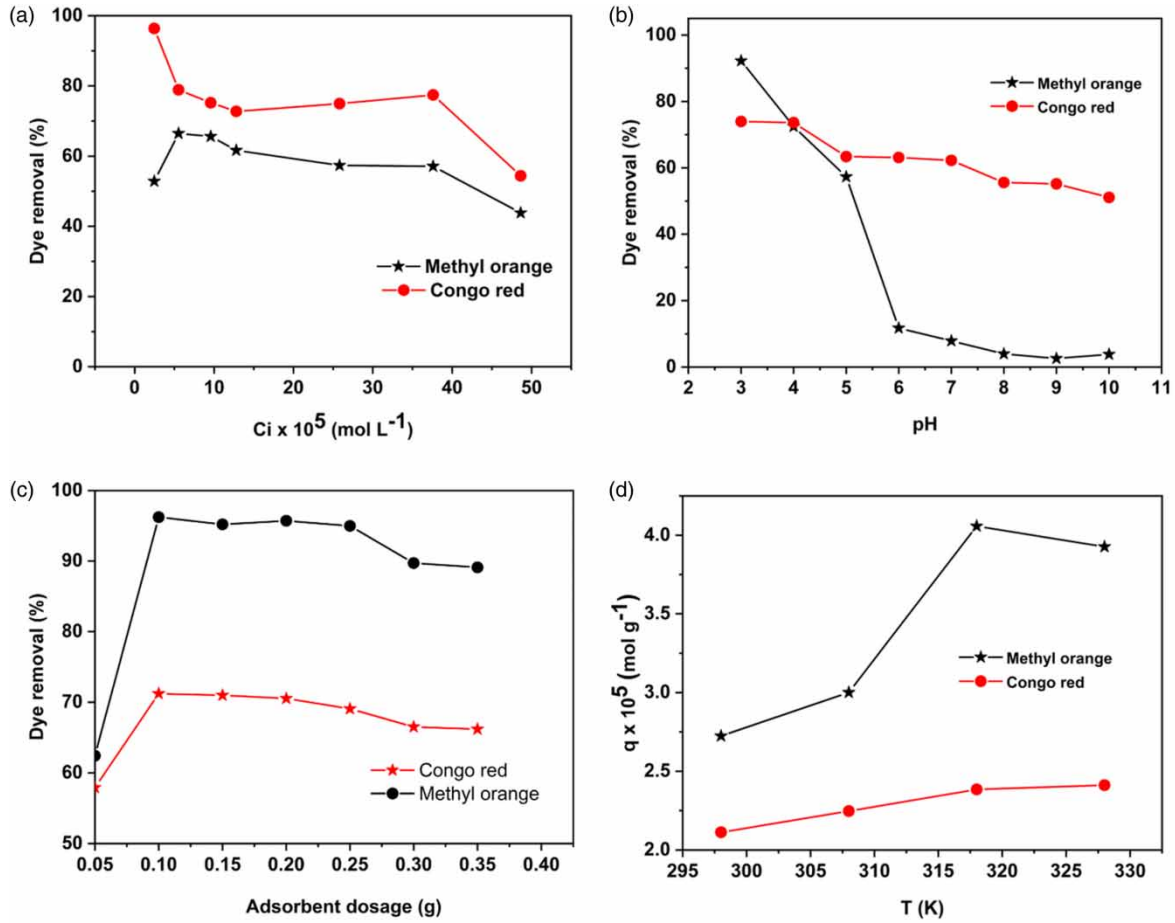

Figure 4 | Initial concentration effect (a), pH (b), adsorbent amount (c), and temperature (298–328 K) (d) of methyl orange and Congo red adsorption onto MnO_2–PVP composite.

These occurrences could be attributed to several factors: (a) At low initial concentration, the availability of vacant pores, and binding sites on PVP-loaded MnO_2 are high. However, the fractional adsorption and mass transfer of methyl orange and Congo red become low, leading to the lower percentage eliminations of azo dyes at initial dye concentrations below 200 mg L^{-1}. (b) As the initial dye concentration increases from 50 mg L^{-1}, the mass transfer force of dye also increases, leading to high adsorption on available binding sites of PVP-loaded MnO_2. (c) As the initial dye concentration further increases above 100 mg L^{-1} and particularly at 200 mg L^{-1}, the ratio of the dye molecules to the available binding sites is at levels that do not support

mass transfer. Moreover, at initial dye concentration, the mass transfer of dye molecules is higher due to the increased methyl orange and Congo red to binding sites ratio; however, the number of available binding sites on the MnO_2–PVP composite will decrease and disappear as the dye molecules occupy them. This results in general lower removal percentages of methyl orange and Congo red at high initial concentrations. Similar results were reported by Guo *et al.* while studying regenerated cellulose/polyethyleneimine composite aerogel for efficient and selective adsorption of anionic dyes (Guo *et al.* 2024).

3.4.2. Effect of pH

The adsorption of dye by PVP-supported MnO_2 is studied in pH ranges from 3 to 10 at 298 K. The adsorbent quantity and initial dye concentration were set at 0.1 g, and 50 mg/L respectively. The removal was decreased with an increase in the pH of the system (Figure 4(b). This decrease at higher pH was due to OH ions on the surface at higher pH and its competition with anionic dyes toward the surface, leading to a decrease in adsorption. On the other hand, at lower pH values, the amine groups of the dye protonated to produce a positive surface, which results repulsion between the dye and surface of the adsorbent. At lower pH values, the dominant electrostatic forces create a connection amid anionic dye and positive surface. On the other hand, the electrostatic force of repulsion leading to decreased adsorption (Arrisujaya *et al.* 2023; Khan *et al.* 2020b).

3.4.3. Effect of adsorbent dosage

The adsorption of azo dyes from 50 mg L^{-1} solution was conducted by changing the adsorbent dosage from 0.05 to 0.4 g. Figure 4(c) shows that the percent removal increases when the amount increases from 0.05 to 0.1 g and remains constant from 0.1 to 0.25 g of adsorbent. The high adsorption is due to the availability of more sites when we go from 0.05 to 0.1 g, but after 0.1 g adsorbent, the agglomeration of adsorbent particles occurred and thus lowering in the adsorption is observed. The mass of 0.1 g of adsorbent was taken as the optimized dose for further experiments. Similar results were reported by Khan *et al.* (2020b).

3.4.4. Effect of temperature

The effect of temperature on the adsorption process is conducted in a range of 298 to 328 K (Figure 4(d). The dye elimination was found to increase with the increase in temperature (298–328 K) for both methyl orange and Congo red. The methyl orange adsorption increased up to 318 K but decreased at 328 K due to a change in surface configuration at a very high temperature. However, the reaction is endothermic when the temperature increased from 298 to 318 K. The high mobility of dyes at high temperature (328 K) is accountable for high adsorption (Naeem *et al.* 2014). A comparison of azo dye adsorption of the reported literature with our adsorbent is shown in Table 5.

Table 5 | Comparison of maximum adsorption capacity of various adsorbents for Congo red removal

Adsorbent	q_m (mg g^{-1})	References
Hierarchical NiO nanosheets	151.7	Cheng *et al.* (2011)
Hierarchical spindle-like γ-Al_2O_3	176.7	Cai *et al.* (2010)
Hollow hierarchical MnO	60	Fei *et al.* (2008)
NiO-SiO_2 hollow microspheres	204	Lei *et al.* (2016)
Hierarchical porous NiO/Al2O_3	186.9	Rong *et al.* (2017)
MnO_2–PVP composite	311	*This study*

3.5. Adsorption isotherms

3.5.1. Langmuir model

The linearized form of the conventional Langmuir adsorption model is written as follows:

$$\frac{C_e}{X} = \frac{1}{K_b X_m} + \frac{C_e}{X_m} \tag{8}$$

where C_e (mol/L) is equilibrium concentration, X_m (mol g^{-1}) is maximum adsorption, X (mol g^{-1}) is adsorbed

amount, and K_b (L g $^{-1}$) is binding energy constant. X_m and K_b values were calculated from the plot between C_e versus C_e/X (Figure 5(a) and 5(b)). The X_m values for both cases are close to experimental values (Table 6), which confirm the applicability Langmuir model. The X_m values of methyl orange are greater than Congo red, which is opposite to their K_b values. It is clear that although methyl orange adsorption is higher than Congo red, its binding to the surface is weaker than Congo red (Mahmood *et al.* 2016; Abdullah *et al.* 2023).

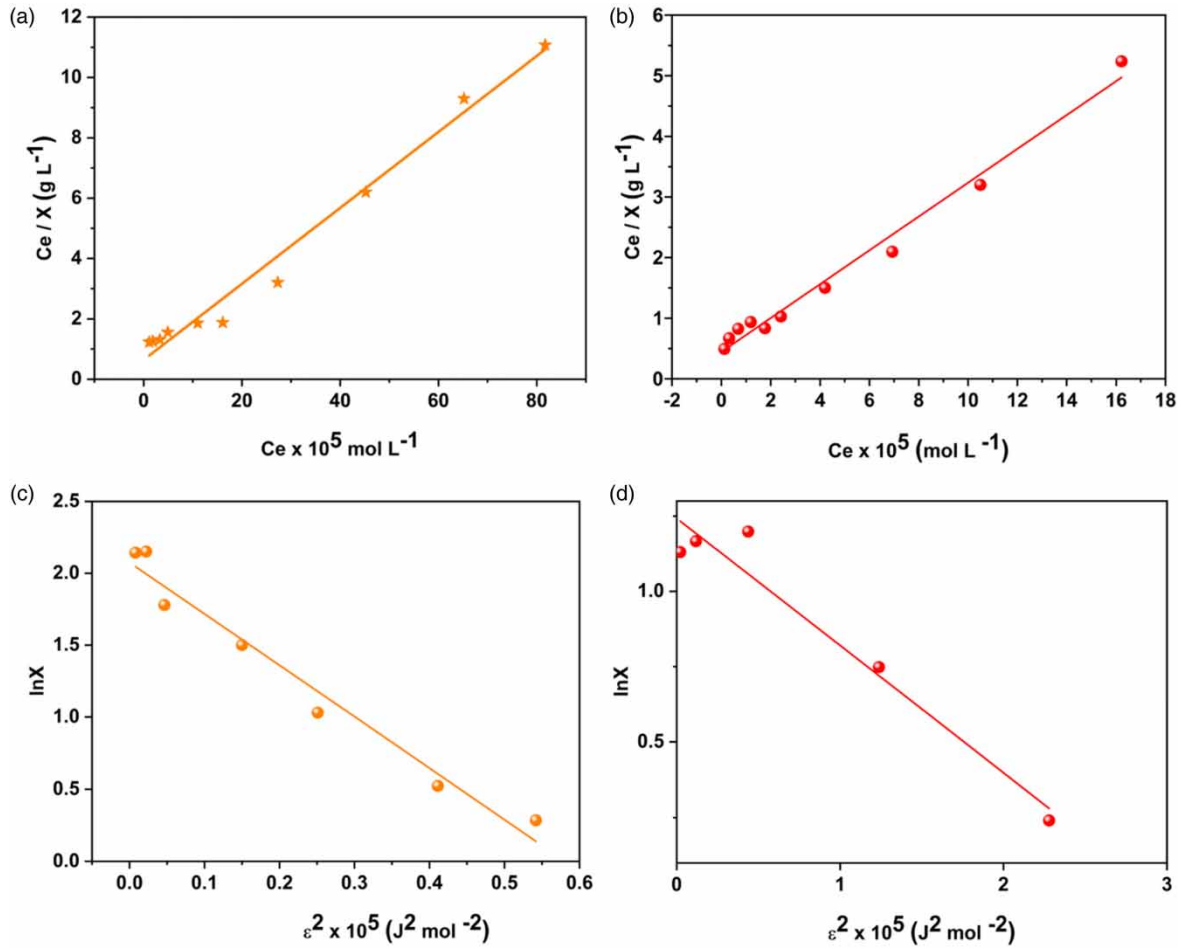

Figure 5 | Langmuir isotherm for methyl orange (a), and Congo red (b), DR plot for methyl orange (c), and Congo red (d) by MnO_2–PVP composite.

Table 6 | Langmuir parameters at 298 K at pH 5

Dye	$X_m \times 10^5$ (mol g^{-1})	K_b (L g^{-1})	R^2
Methyl orange	8.396	13,992	0.96
Congo red	3.396	84,646	0.977

3.5.2. Dubinin–Radushkevich model

The current data are introduced to the Dubinin–Radushkevich (DR) isotherm, which is shown as follows:

$$\ln X = \ln qX_m - K\varepsilon^2 \tag{9}$$

where X is adsorbed dye at equilibrium, X_m is saturation capacity, C_e is equilibrium concentration (mol L^{-1}), ε is

the Polanyi potential, which is equal to RT $\ln(1 + 1/C_e)$, K is the energy constant, and R is the gas constant. A plot of ln X versus ε^2 gives a linear relationship with high correlation coefficients (Figure 5(c) and 5(d)). K_d values obtained from DR models are applied for the calculation of mean free energy (E):

$$E = -(2k)^{-0.5} \tag{10}$$

Equation 10 was applied to find E. The mean adsorption energy was 1.088 for Congo red, while 1.27 (kJ mol^{-1}) for methyl orange, which gives information regarding the mechanisms of the process. If the E values are in the range of 8–16 kJ mol^{-1}, the adsorption process is chemical in nature, and when E is less than 8 kJ mol^{-1}, then the process in physical in nature. Herein, in both cases, the values of E are less than 8 (Table 7), which confirms the physical adsorption (Mahmood *et al.* 2014).

Table 7 | DR parameters for at 298 K at pH 5

Dye	E (kJ mol^{-1})	R^2
Methyl orange	1.271	0.96
Congo red	1.088	0.95

3.6. Thermodynamics study

The thermodynamics factors are computed by the following relationships:

$$K_c = \frac{X}{C_e} \tag{11}$$

$$\ln K_c = \frac{\Delta S}{R} - \frac{\Delta H}{RT} \tag{12}$$

where K_c is the constant. The Gibbs free energy (ΔG) is calculated from Equation (13):

$$\Delta G = \Delta H - T\Delta S \tag{13}$$

The changes in entropy and enthalpy for dyes were calculated from the plot of $\ln K_c$ versus $1/T$ (Figure 6(a) and 6(b), respectively). The negative values of free energy changes show the spontaneous nature of the process (Tables 8 and 9). The decrease in values of ΔG with the increased temperature (298–328 K) further demonstrates that the adsorption process is favorable at high temperature (328 K).

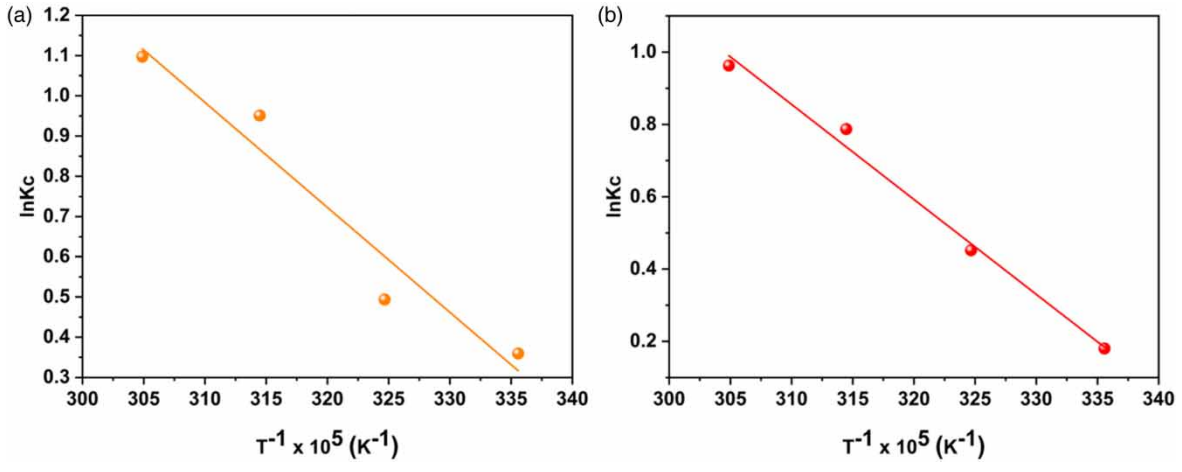

Figure 6 | ln K_c versus T^{-1} for methyl orange (a) and Congo red (b) at pH 5.

Table 8 | Thermodynamics parameters of methyl orange

Temperature (K)	ΔG (kJ mol^{-1})	ΔH (kJ mol^{-1})	ΔS (J mol^{-1} K^{-1})
298	−22.46	21.6	75.38
308	−23.21		
318	−23.97		
328	−24.72		

Table 9 | Thermodynamics parameters of Congo red

Temperature (K)	ΔG (kJ mol^{-1})	ΔH (kJ mol^{-1})	ΔS (J mol^{-1} K^{-1})
298	−0.50	21.8	66.96
308	−1.17		
318	−1.84		
328	−2.51		

Moreover, the lower negative value of ΔG is observed for Congo red compared to methyl orange, demonstrating that Congo red adsorption is energetically less favorable. The positive values of ΔS (66.96 and 75.38 J mol^{-1} K^{-1}) for Congo red and methyl orange, respectively, are due to the high randomness, which confirms a good affinity of dyes toward the surface. The positive values of ΔS also reveal that the arrangement of dye molecules on solid – solution interface turns into more randomness. The positive ΔH value confirms an endothermic process (Khan *et al.* 2020b).

4. CONCLUSION

The adsorption efficiency of the MnO_2–PVP composite toward azo dyes was considerably enhanced compared to MnO_2, which confirms the role of polymer in composite materials. The successful interaction of PVP with MnO_2 is confirmed by the FTIR analysis and other techniques. The high value of the binding energy constant (K_b) in the case of PVP-loaded MnO_2 composite as compared to MnO_2 is evidence of greater affinity of the dye toward the composite adsorbent. Kinetically adsorption was followed by film diffusion and intraparticle diffusion. The thermodynamic investigations confirm that the dye adsorption process was endothermic, spontaneous, and physical in nature. The MnO_2–PVP composite can be utilized as the best adsorbent for wastewater treatment through adsorption.

AUTHOR CONTRIBUTION

Afsar Khan (first and corresponding author): experiments and writing – original draft; Muhammad Arif (second corresponding author): experiments and revision; Zhengwei Han: writing and review; Yu Xie: graphs and tables and manuscript revision; Chenquan Ni: editing.

DATA AVAILABILITY STATEMENT

All relevant data are included in the paper or its Supplementary Information.

CONFLICT OF INTEREST

The authors declare there is no conflict.

REFERENCES

Abdullah, N. H., Nizam, W. H. A., Norhisham, M. H. I., Husaimi, N. A., Ngadiman, N., Salim, N. A. A., Abu Hassan, N. & Muslim, N. H. 2023 Phosphorus removal from ore waste in aqueous solution with different mass of ore waste adsorbent from the Johor mine site. *Water Practice Technology* **18**(11), 2957–2970.

Abugu, H. O., Alum, O. L., Ihedioha, J. N., Ezugwu, A. L., Ucheana, I. A., Ali, I. J. & Eze, S. I. 2023 Sequestration of Pb2 + from aqueous solution using bio-based-alkaline modified sorbent from waste *Irvingia gabonensis* seed husk. *Water Practice Technology* **18**(11), 2495–2513.

Aliabadi, R. S. & Mahmoodi, N. 2018 Synthesis and characterization of polypyrrole, polyaniline nanoparticles and their nanocomposite for removal of azo dyes; sunset yellow and Congo red. *Journal of Cleaner Production* **179**, 235–245.

Alsbaiee, A., Smith, B. J., Xiao, L., Ling, Y., Helbling, D. E. & Dichtel, W. R. 2016 Rapid removal of organic micropollutants from water by a porous β-cyclodextrin polymer. *Nature* **529**(75), 190–194.

Arrisujaya, D., Utami, N. S., Mulyawati, T., Rahmalisa, D., Wati, S. & Hidayat, H. 2023 Chromium (VI) and lead (II) adsorption using *Mangifera kemanga* leaves. *Water Practice Technology* **18**(11), 2785–2796.

Bhatnagar, A. & Jain, A. 2005 A comparative adsorption study with different industrial wastes as adsorbents for the removal of cationic dyes from water. *Journal of Colloid and Interface Science* **281**(1), 49–55.

Cai, W., Yu, J. & Jaroniec, M. 2010 Template-free synthesis of hierarchical spindle-like γ-Al_2O_3 materials and their adsorption affinity towards organic and inorganic pollutants in water. *Journal of Materials Chemistry* **20**(22), 4587–4594.

Cheng, B., Le, Y., Cai, W. & Yu, J. 2011 Synthesis of hierarchical Ni $(OH)_2$ and NiO nanosheets and their adsorption kinetics and isotherms to Congo red in water. *Journal of Hazardous Materials* **185**(3), 889–897.

Fei, J., Cui, Y., Yan, X., Qi, W., Yang, Y., Wang, K., He, Q. & Li, J. 2008 Controlled preparation of MnO_2 hierarchical hollow nanostructures and their application in water treatment. *Advanced Materials* **20**(3), 452–456.

Guo, J., Zhou, S., Ma, X., He, S., Chen, D., Xie, F., Wang, C., Yang, H. & Li, W. 2024 Regenerated cellulose/polyethyleneimine composite aerogel for efficient and selective adsorption of anionic dyes. *Separation Purification Technology* **330**(1), 125480.

Kabuba, J. & Banza, M. 2021 Modification of clinoptilolite with dialkylphosphinic acid for the selective removal of cobalt (II) and nickel (II) from hydrometallurgical effluent. *The Canadian Journal of Chemical Engineering* **99**(2), 168–178.

Khan, A., Naeem, A. & Mahmood, T. 2020a Kinetic studies of methyl orange and Congo red adsorption and photocatalytic degradation onto PVP-Functionalized ZnO. *Kinetics and Catalysis* **61**(5), 730–739.

Khan, A., Naeem, A. & Mahmood, T. 2020b Thermodynamic study of adsorption of methyl orange and Congo red from aqueous solutions by PVP-Functionalized ZnO. *Russian Journal of Physical Chemistry A* **94**(8), 1581–1586.

Khan, A., Naeem, A., Mahmood, T., Muhammad, N. & Hussain, S. 2022 Fixed-bed column adsorption of methyl orange by poly (vinyl pyrrolidone)-functionalized manganese oxide. *Journal of Chemical Technology & Biotechnology* **97**(10), 2898–2903.

Kim, H. & Popov, B. N. 2003 Synthesis and characterization of MnO_2-based mixed oxides as supercapacitors. *Journal of the Electrochemical Society* **150**(3), 150–156.

Lei, C., Zhu, X., Zhu, B., Yu, J. & Ho, W. 2016 Hierarchical NiO–SiO_2 composite hollow microspheres with enhanced adsorption affinity towards Congo red in water. *Journal of Colloid Interface Science* **466**, 238–246.

Li, Y., Wang, Z., Huang, B., Dai, Y., Zhang, X. & Qin, X. 2015 Synthesis of BiOBr-PVP hybrids with enhanced adsorption-photocatalytic properties. *Applied Surface Science* **347**, 258–264.

Mahmood, T., Din, S., Naeem, A., Tasleem, S., Alum, A. & Mustafa, S. 2014 Kinetics, equilibrium and thermodynamics studies of arsenate adsorption from aqueous solutions onto iron hydroxide. *Journal of Industrial and Engineering Chemistry* **20**(5), 3234–3242.

Mahmood, T., Khan, A., Naeem, A., Hamayun, M., Muska, M., Farooq, M. & Hussain, F. 2016 Adsorption of Ni (II) ions from aqueous solution onto a fungus *Pleurotus ostreatus*. *Desalination and Water Treatment* **57**(16), 7209–7218.

Miyittah, M. K., Tsyawo, F. W., Kumah, K. K., Stanley, C. D. & Rechcigl, J. E. 2016 Suitability of two methods for determination of point of zero charge (PZC) of adsorbents in soils. *Communications in Soil Science and Plant Analysis* **47**(1), 101–111.

Mon, M., Bruno, R., Tiburcio, E., Viciano-Chumillas, M., Kalinke, L. H., Ferrando-Soria, J. s., Armentano, D. & Pardo, E. 2019 Multivariate metal–organic frameworks for the simultaneous capture of organic and inorganic contaminants from water. *Journal of the American Chemical Society* **141**(34), 13601–13609.

Naeem, A., Khan, A., Mahmood, T., Muska, M., Din, S. U., Khan, M. S., Hamayun, M. & Waseem, M. 2014 Kinetics, equilibrium and thermodynamic studies of Mn (II) biosorption from aqueous solution onto *Pleurotus ostreatus*. *Journal of Chemical Society of Pakistan* **36**(5), 788–792.

Naseem, K., Farooqi, Z. H., Begum, R. & Irfan, A. 2018 Removal of Congo red dye from aqueous medium by its catalytic reduction using sodium borohydride in the presence of various inorganic nano-catalysts: A review. *Journal of Cleaner Production* **187**, 296–307.

Nuengmatcha, P., Kuyyogsuy, A., Porrawatkul, P., Pimsen, R., Chanthai, S. & Nuengmatcha, P. 2023 Efficient degradation of dye pollutants in wastewater via photocatalysis using a magnetic zinc oxide/graphene/iron oxide-based catalyst. *Water Science Engineering* **16**(3), 243–251.

Oladoye, P. O., Ajiboye, T. O., Wanyonyi, W. C., Omotola, E. O. & Oladipo, M. E. 2023 Insights into remediation technology for malachite green wastewater treatment. *Water Science Engineering* **16**(3), 261–270.

Özacar, M. & Şengil, İ. A. 2005 A kinetic study of metal complex dye sorption onto pine sawdust. *Process Biochemistry* **40**(2), 565–572.

Parveen, K. & Rafique, U. 2018 Development of cobalt-doped alumina hybrids for adsorption of textile effluents. *Adsorption Science & Technology* **36**(1–2), 182–197.

Rong, J., Zhang, T., Qiu, F. & Chen, M. 2017 Structural evolution of hierarchical porous NiO/Al_2O_3 composites and their application for removal of dyes by adsorption. *Korean Journal of Chemical Engineering* **34**, 41–53.

Rose, P. A., Praseetha, P., Bhagat, M., Alexander, P., Abdeen, S. & Chavali, M. 2013 Drug embedded PVP coated magnetic nanoparticles for targeted killing of breast cancer cells. *Technology in Cancer Research & Treatment* **12**(5), 463–472.

Saeed, T., Naeem, A., Mahmood, T., Khan, A., Ahmad, Z., Hamayun, M., Khan, I. W. & Khan, N. H. 2021 Kinetic and thermodynamic studies of polyvinyl chloride composite of manganese oxide nanosheets for the efficient removal of dye from water. *Water Science Technology* **84**(4), 851–864.

Song, Y., Shang, M., Li, J. & Su, Y. 2021 Continuous and controllable synthesis of MnO_2/PPy composites with core–shell structures for supercapacitors. *Chemical Engineering Journal* **405**, 127059.

Venkatesha, T., Viswanatha, R., Nayaka, Y. A. & Chethana, B. 2012 Kinetics and thermodynamics of reactive and vat dyes adsorption on MgO nanoparticles. *Chemical Engineering Journal* **198**, 1–10.

Yuan, L., Wan, C. & Zhao, L. 2015 Facial in-situ synthesis of MnO_2/PPy composite for supercapacitor. *International Journal of Electrochemical Science* **10**(11), 9456–9465.

Zhang, L., Shao, Q. & Xu, C. 2019 Enhanced azo dye removal from wastewater by coupling sulfidated zero-valent iron with a chelator. *Journal of Cleaner Production* **213**, 753–761.

First received 27 November 2023; accepted in revised form 26 January 2024. Available online 13 February 2024